Nonlinear, dissipative, planar Nearfield Acoustical Holography based on Westervelt wave equation ☆

Yaying Niu, Yong-Joe Kim*

Acoustics and Signal Processing Laboratory, Department of Mechanical Engineering, Texas A&M University, 3123 TAMU, College Station, TX 77843-3123, USA

ARTICLE INFO

ABSTRACT

When a conventional, linear, lossless Nearfield Acoustical Holography (NAH) procedure is applied to reconstruct three-dimensional (3-D) sound fields that are radiated from a high-level noise source and include significant nonlinear components, it can result in significant reconstruction errors. Here, a nonlinear, dissipative, planar NAH procedure is introduced that can be used to identify nonlinear noise characteristics in the 3-D nearfield of a high-level noise source from two-dimensional (2-D) sound pressure data measured on a hologram surface. The proposed NAH procedure is derived by applying perturbation and renormalization methods to the nonlinear, dissipative Westervelt wave equation. In order to validate the proposed procedure, the nonlinear and dissipative sound pressure fields radiated from a high-level pulsating sphere and an infinite-size, vibrating panel are calculated from the Burgers equations in the spherical and rectangular coordinates, respectively. An improved SONAH procedure is applied to reconstruct source sound pressure fields that are input to the proposed nonlinear NAH projection procedure. Within 2.5 m nearfield reconstruction distance from the pulsating sphere, the nonlinear sound pressure field reconstructed by applying the proposed NAH procedure matches well with the directly-calculated field at the maximum reconstruction error of 0.6 dB. In the infinite-size panel case, the reconstructed nonlinear sound pressure field agrees also well with the directly-calculated result with the maximum reconstruction error of 1 dB.

© 2012 Elsevier Ltd. All rights reserved.

1. Introduction

For the purpose of identifying sound sources and visualizing their sound radiation patterns in a three-dimensional (3-D) space, a Nearfield Acoustical Holography (NAH) procedure can be used to linearly project the sound pressure data measured on a two-dimensional (2-D) measurement surface (i.e., hologram surface) into a 3-D space. The NAH procedure that includes evanescent wave components (i.e., subsonic wave components) to improve the spatial resolution of a reconstructed sound field was first introduced by Williams et al. in 1980s [1–3]. Since then, many researchers have improved the NAH procedure and applied the improved procedures to various vibroacoustic and aeroacoustic problems although their applications are limited to "linear" acoustic problems [4–10].

The sound fields radiated from high-level noise sources include significant nonlinear components that can lead to shock wave propagations. Thus, it is critical to identify noise propagation characteristics in the nearfield of the sources in order to design optimal noise control schemes to suppress the nonlinear noise components before they turn into shock waves. However, the conventional, linear, lossless NAH procedures in Refs. [1–10] cannot be used to visualize the highly nonlinear and dissipative sound fields correctly. Therefore, it is here proposed to develop a novel, nonlinear, dissipative, planar NAH procedure to consider the nonlinear and thermoviscous effects. Combined with a linear and lossless NAH procedure, the proposed NAH procedure can be used to nonlinearly project the sound pressure data measured on a 2-D planar measurement surface close to the noise sources into a 3-D space to visualize both linear and nonlinear acoustic fields.

Hamilton and Blackstock [11] summarized nonlinear acoustics research work done by many researchers [12–21]. In particular, Ginsberg [15–18] and Nayfeh [19–21] used perturbation and renormalization methods to investigate nonlinear acoustic wave propagations in planar, cylindrical, and spherical cases. According to their investigations on 2-D planar nonlinear wave propagation based on the perturbation and renormalization procedures, particle velocity components along a wave propagating direction can advance or retard wavefronts, while the transverse particle velocity components can bend the rays of the nonlinear waves [15,16,19,20]. For a spherical wave, however, transverse particle velocity decays in proportional to $1/r$ compared to the radial velocity [21]. Thus, the bending of the spherical wave ray is negligible and the ray remains straight. For a 1-D nonlinear planar wave, the transverse particle velocity is zero and thus the ray is straight along the wave propagating direction.

Among nonlinear and thermoviscous acoustic equations for perfect gases [11], the Westervelt wave equation (WWE) [11,13] is selected to derive the proposed nonlinear and dissipative NAH procedure. The WWE is solved by using perturbation and modified renormalization methods to give linear and nonlinear NAH reconstructed sound pressure fields that include the nonlinearity-induced steepening effects of wavefronts but exclude the transverse-particle-velocity-induced bending of rays. Thus, the proposed nonlinear NAH procedure can be applied to nonlinear wave propagation problems only with straight rays: e.g., spherical and 1-D planar wave cases. In addition, the "local" nonlinearity caused by high-level source surface displacements is not included in the WWE. That is, the WWE is appropriate to describe sound waves only with dominant "cumulative" nonlinearity apart from a noise source surface.

It is here proposed that the WWE-based NAH procedure is derived in an open 3-D space. The anechoic boundary condition is then applied at the infinite boundary of the open 3-D space. An acoustic pressure boundary condition is also applied on a planar measurement surface. Then, through the linear, backward projection combined with the WWE-based, nonlinear, forward projections, acoustic pressure fields in the 3-D space can be related to the acoustic pressure boundary condition on the measurement surface. Fig. 1 shows the example of a semi-anechoic 3-D space to measure the jet noise of a military fighter airplane. The rigid acoustic boundary condition is applied on the ground surface and the non-reflective acoustic boundary condition, at the infinite boundary, $r = \infty$. In Fig. 1, acoustic pressure transducers are placed on the planar measurement surface to obtain the acoustic pressure boundary condition.

The proposed nonlinear and dissipative NAH procedure is valid only for monofrequency source cases. Thus, the first-order, linear sound pressure at a single excitation frequency is used to calculate the second-order, nonlinear sound pressure at twice of this excitation frequency. In multi-frequency source cases, however, Fenlon's solution [11,14] indicates that each frequency component consists of the harmonics, summations, or differences of other frequency components. Thus, the excitation frequency component can include nonlinear components and cannot be directly applied for the calculation of its second-order nonlinear component.

Numerical simulations with a nonlinear and dissipative pulsating sphere and an infinite-size panel are performed to validate the proposed NAH procedure. Here, the Burgers equations [11] are solved in the spherical and rectangular coordinates to obtain the nonlinear and dissipative sound pressure fields radiated from the high-level pulsating sphere and the infinite-size panel, respectively. The calculated hologram data are backward projected to the source surface, and then the reconstructed source data are input to the proposed, nonlinear, forward, NAH projection procedure. The sound
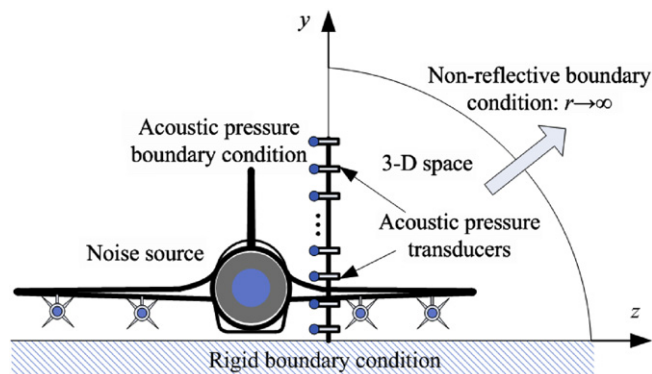

Fig. 1. Example of open 3-D space with rigid, non-reflective, and acoustic pressure boundary conditions.

pressure fields reconstructed by using the proposed NAH procedure are compared with the directly-calculated sound pressure fields.

2. Theory

The overall procedure of the proposed nonlinear NAH is presented as a flowchart in Fig. 2. The steps in Fig. 2 will be described in the following sections.

2.1. Perturbation procedure for Westervelt wave equation

The nonlinear and dissipative Westervelt wave equation (WWE) [11,13] is represented as

$$\nabla^2 p - \frac{1}{c_0^2}\frac{\partial^2 p}{\partial t^2} = -\frac{b}{c_0^4}\frac{\partial^3 p}{\partial t^3} - \frac{\beta}{\rho_0 c_0^4}\frac{\partial^2 p^2}{\partial t^2}, \tag{1}$$

where $\beta = (\gamma+1)/2$ is the nonlinearity coefficient for an ideal gas and b is the sound diffusivity that includes viscous and thermal conduction effects [11,12]: i.e.,

$$b = \frac{1}{\rho_0}\left(\frac{4}{3}\mu + \eta\right) + \frac{\kappa}{\rho_0}\left(\frac{1}{C_v} - \frac{1}{C_p}\right) = \nu\left(\frac{4}{3} + \frac{\eta}{\mu} + \frac{\gamma-1}{\mathrm{Pr}}\right). \tag{2}$$

In Eqs. (1) and (2), p is the acoustic pressure, ρ_0 is the ambient fluid medium density, c_0 is the speed of sound, μ and η are the shear and bulk viscosities, respectively, κ is the thermal conductivity, C_v and C_p are the heat capacities at constant volume and constant pressure, respectively, $\nu = \mu/\rho_0$ is the kinematic viscosity, $\gamma = C_p/C_v$ is the specific heat capacity ratio, and $\mathrm{Pr} = \mu C_p/\kappa$ is the Prandtl number. The two terms on the right-hand side (RHS) of Eq. (1) thus represent thermoviscous dissipation and cumulative nonlinear effects, respectively.

By using the perturbation method [11,15–21], the acoustic pressure, p in the Cartesian coordinates, (x, y, z) can be expanded as

$$p(x,y,z,t) = O(\varepsilon) + O(\varepsilon^2) + \cdots = p_1(x,y,z,t) + p_2(x,y,z,t) + \cdots, \tag{3}$$

where ε is the small perturbation parameter (e.g., acoustic Mach number, $\varepsilon = u_1/c_0$ where u_1 is the magnitude of acoustic particle velocity) and p_n is the nth order acoustic pressure ($n=1,2,3,\ldots$). The sound diffusivity, b in Eq. (2) is a small number in the order of ε in air [11]. By substituting p in Eqs. (3) into (1) and neglecting the $O(\varepsilon^3)$ and higher-order small terms, the first- and second-order equations can be associated with the $O(\varepsilon)$ and $O(\varepsilon^2)$ terms, respectively. The resulting first- and second-order equations are then represented as

$$\nabla^2 p_1 - \frac{1}{c_0^2}\frac{\partial^2 p_1}{\partial t^2} = 0, \tag{4a}$$

$$\nabla^2 p_2 - \frac{1}{c_0^2}\frac{\partial^2 p_2}{\partial t^2} = -\frac{b}{c_0^4}\frac{\partial^3 p_1}{\partial t^3} - \frac{\beta}{\rho_0 c_0^4}\frac{\partial^2 p_1^2}{\partial t^2}. \tag{4b}$$

The third- and higher-order sound pressure components have negligibly small amplitudes even at an extremely high noise level when compared to the first- and second-order acoustic pressure components. It is thus sufficient to describe the nonlinear and thermoviscous effects by using the only first- and second-order sound pressure components. The first-order equation in Eq. (4a) is a linear, lossless, homogeneous wave equation and the second-order equation in Eq. (4b) is a nonlinear, dissipative, inhomogeneous wave equation. The left-hand side (LHS) of Eq. (4b) is a linear wave equation with
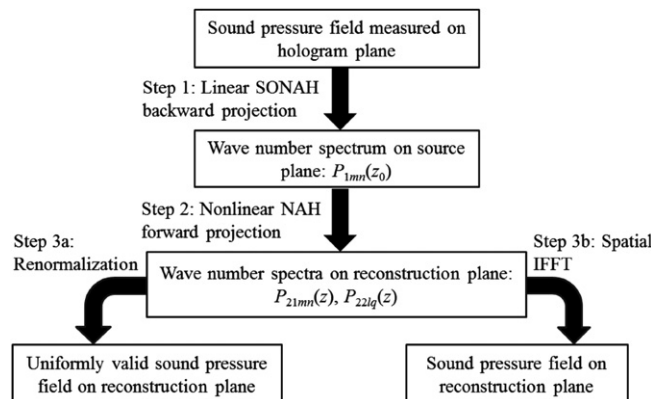

Fig. 2. Flowchart of nonlinear NAH procedure.

the unknown of the second-order pressure, p_2, while the RHS consists of the dissipative and nonlinear source terms that are composed of the first-order acoustic pressure, p_1. Thus, once the first-order sound pressure solution is obtained from Eq. (4a), the second-order equation becomes a linear, inhomogeneous partial differential equation of which solution can be obtained analytically for certain cases.

2.2. Nonlinear, dissipative, planar NAH projection

In the current nonlinear and dissipative NAH algorithm, the hologram sound pressure data is assumed to be measured close to the sound source surface and thus linear components are much more dominant than nonlinear components. In practical measurements of sound pressure fields generated by a monofrequency sound source, the measured sound pressure data at this single fundamental frequency contain only first-order, linear sound pressure components. The linear NAH algorithms [1–10] can be thus applied to the backward projection from the hologram surface to the sound source surface at the fundamental frequency. Here, the improved Statistically Optimal Nearfield Acoustical Holography (SONAH) algorithm [10] is applied to backward project the hologram sound pressure field at $z=z_h$ to the source surface at $z=z_0$. As described in Ref. [10], this improved SONAH procedure can significantly reduce the truncation errors at measurement aperture edges. Thus, it allows accurately reconstructing a source sound pressure field even with the hologram data measured by using a microphone array with a small measurement aperture. This SONAH backward projection procedure is also indicated as the first step in Fig. 2. The linearly reconstructed sound pressure field on the source plane is then input to the nonlinear and dissipative NAH forward projection procedure.

For the forward projection, cumulative nonlinear and thermoviscous effects become more significant as sound wave propagates further to the farfield of a noise source [11]. This forward projection is the second step in Fig. 2 and described in the following derivation procedure in an open 3-D space (i.e., free field) where there is no wave reflected from the infinite boundary (i.e., anechoic boundary condition). A semi-anechoic condition can be also considered by mirroring the measured sound pressure data with respect to the rigid surface (see Fig. 1) and combining the original and mirrored data. The combined data can be then projected as in a free field.

In the Cartesian coordinates, (x,y,z), the acoustic pressure solution of Eq. (4a) at the fundamental frequency of ω can be obtained from the conventional, linear, planar NAH projection [1–3] in a discretized form as

$$p_1(x,y,z,t) = \mathrm{Re}\left(\frac{1}{N_x N_y}\sum_{m=0}^{N_x-1}\sum_{n=0}^{N_y-1} P_1(k_{xm},k_{yn},z_0,\omega)\mathrm{e}^{\mathrm{i}m\Delta k_x x}\mathrm{e}^{\mathrm{i}n\Delta k_y y}\mathrm{e}^{\mathrm{i}k_{zmn}(z-z_0)}\mathrm{e}^{-\mathrm{i}\omega t}\right), \tag{5}$$

where z_0 and z are the source and reconstruction surface locations ($z \geq z_0$), respectively, N_x and N_y are the number of measurement points along the x- and y-directions, respectively, and $(k_{xm},k_{yn})=(m\Delta k_x,n\Delta k_y)$ are the discrete wave numbers. The x- and y-direction wave number intervals are determined by the following equations:

$$\Delta k_x = 2\pi/L_x = 2\pi/(N_x\Delta x), \tag{6a}$$

$$\Delta k_y = 2\pi/L_y = 2\pi/(N_y\Delta y), \tag{6b}$$

where Δx and Δy are the sampling spaces in the x- and y-directions, respectively. In Eq. (5), the wave number spectrum, $P_1(k_{xm},k_{yn},z_0,\omega)=P_{1mn}$, is obtained by applying the spatial Fast Fourier Transform (FFT) to the source sound pressure data, $p_1(x,y,z_0,\omega)$ that is obtained by applying the linear, backward SONAH projection to the measured sound pressure data at $z=z_h$ (see the first step in Fig. 2). The projection relation between the reconstruction and source surfaces is represented as

$$P_1(m,n,z,\omega) = P_1(m,n,z_0,\omega)\mathrm{e}^{\mathrm{i}k_{zmn}(z-z_0)} \tag{7}$$

In Eq. (7), the z-direction wave number, k_{zmn} is the function of ω, k_{xm}, and k_{yn}: i.e.,

$$k_{zmn}^2 = k^2-(m\Delta k_x)^2-(n\Delta k_y)^2, \tag{8}$$

where $k=\omega/c_0$ is the acoustic wave number. By substituting Eqs. (5) into (4b), the inhomogeneous source terms on the RHS of Eq. (4b) are represented as

$$\frac{\partial^3 p_1}{\partial t^3} = \mathrm{Re}\left(\frac{\mathrm{i}\omega^3}{N_x N_y}\sum_{m=0}^{N_x-1}\sum_{n=0}^{N_y-1} P_{1mn}\mathrm{e}^{\mathrm{i}m\Delta k_x x}\mathrm{e}^{\mathrm{i}n\Delta k_y y}\mathrm{e}^{\mathrm{i}k_{zmn}(z-z_0)}\mathrm{e}^{-\mathrm{i}\omega t}\right), \tag{9}$$

$$\frac{\partial^2 p_1^2}{\partial t^2} = \frac{1}{2}\mathrm{Re}\left(\frac{-4\omega^2}{N_x^2 N_y^2}\sum_{l=0}^{N_x-1}\sum_{q=0}^{N_y-1}\mathrm{e}^{\mathrm{i}l\Delta k_x x}\mathrm{e}^{\mathrm{i}q\Delta k_y y}\left[\sum_{m=0}^{N_x-1}\sum_{n=0}^{N_y-1} P_{1mn}P_{1(l-m)(q-n)}\mathrm{e}^{\mathrm{i}(k_{zmn}+k_{z(l-m)(q-n)})(z-z_0)}\right]\mathrm{e}^{-\mathrm{i}2\omega t}\right). \tag{10}$$

In Eq. (10), the high wave number components (i.e., $l \geq N_x$ and $q \geq N_y$) are set to zero since they are the subsonic components decaying out exponentially during the forward projections along the z-direction. Similarly, the P_1 and k_z terms with the subscripts of $(l-m)(q-n)$ have only non-zero values when the subscripts, $(l-m)$ and $(q-n)$ are within $[0, N_x-1]$ and $[0, N_y-1]$, respectively. By plugging Eqs. (9) and (10) into (4b) and writing the second-order acoustic pressure solution

as $p_2 = \text{Re}(p_{21}e^{-i\omega t} + p_{22}e^{-i2\omega t})$, Eq. (4b) can be decomposed into two inhomogeneous Helmholtz equations: i.e.,

$$\left(\nabla^2 + k^2\right)p_{21}(x,y,z) = -\frac{ib\omega^3}{N_x N_y c_0^4}\sum_{m=0}^{N_x-1}\sum_{n=0}^{N_y-1}e^{im\Delta k_x x}e^{in\Delta k_y y}\left[P_{1mn}e^{ik_{zmn}(z-z_0)}\right], \tag{11}$$

$$\left(\nabla^2 + 4k^2\right)p_{22}(x,y,z) = \frac{2\beta\omega^2}{N_x^2 N_y^2 \rho_0 c_0^4}\sum_{l=0}^{N_x-1}\sum_{q=0}^{N_y-1}e^{il\Delta k_x x}e^{iq\Delta k_y y}\left[\sum_{m=0}^{N_x-1}\sum_{n=0}^{N_y-1}P_{1mn}P_{1(l-m)(q-n)}e^{i(k_{zmn}+k_{z(l-m)(q-n)})(z-z_0)}\right]. \tag{12}$$

In Eqs. (11) and (12), p_{21} is associated with the "dissipative" sound pressure component at the frequency of ω while p_{22} corresponds to the cumulative "nonlinear" sound pressure component at the frequency of 2ω.

The solution of $p_{21}(x, y, z)$ in Eq. (11) can be assumed as

$$p_{21}(x,y,z) = \sum_{m=0}^{N_x-1}\sum_{n=0}^{N_y-1}P_{21mn}(z)e^{im\Delta k_x x}e^{in\Delta k_y y}. \tag{13a}$$

By substituting Eqs. (13a) into (11), the wave number spectrum, P_{21mn} can be represented as

$$P_{21mn}(z) = -\frac{ib\omega^3(z-z_0)P_{1mn}}{i2N_x N_y c_0^4 k_{zmn}}e^{ik_{zmn}(z-z_0)}. \tag{13b}$$

In Eq. (13), homogeneous solutions are neglected to consider the only particular solution since the transient responses associated with the homogeneous solutions decay out quickly. Thus, the steady-state response represented by the particular solution is only of interest. Reflective waves propagating in the negative z-direction are also neglected in Eq. (13) since no reflection occurs at the infinite boundary of the open 3-D space. Eq. (13) also satisfies the assumption that there is negligible "dissipation" at the source surface: i.e., $P_{21mn}(z_0)=0$. Since there is a $(z-z_0)$ term in Eq. 13(b), the dissipative sound pressure spectrum, $P_{21mn}(z)$ increases as z increases in the supersonic wavenumber region, i.e., $(k_{xm})^2+(k_{yn})^2 < k^2$. Therefore, a renormalization procedure is required to remove this secular term to obtain a uniformly valid solution.

Similar to the aforementioned solution procedure for p_{21}, the solution of $p_{22}(x, y, z)$ in Eq. (12) can be assumed as

$$p_{22}(x,y,z) = \sum_{l=0}^{N_x-1}\sum_{q=0}^{N_y-1}P_{22lq}(z)e^{il\Delta k_x x}e^{iq\Delta k_y y}. \tag{14a}$$

In Eq. (14a), the nonlinear wave number spectrum, P_{22lq} is represented as

$$P_{22lq}(z) = \left[\begin{array}{ll}\dfrac{2\beta\omega^2}{N_x^2 N_y^2 \rho_0 c_0^4}\dfrac{(z-z_0)e^{ik_{2zlq}(z-z_0)}}{2ik_{2zlq}}P_{1(l/2)(q/2)}^2 & \text{when } l=2m \quad \text{and} \quad q=2n \\[2ex] \dfrac{2\beta\omega^2}{N_x^2 N_y^2 \rho_0 c_0^4}\displaystyle\sum_{m=0}^{N_x-1}\sum_{n=0}^{N_y-1}P_{1mn}P_{1(l-m)(q-n)}\left\{\dfrac{e^{i(k_{zmn}+k_{z(l-m)(q-n)})(z-z_0)}-e^{ik_{2zlq}(z-z_0)}}{(k_{2zlq})^2-(k_{zmn}+k_{z(l-m)(q-n)})^2}\right\} & \text{otherwise,}\end{array}\right] \tag{14b}$$

where

$$k_{2zlq}^2 = 4k^2 - (l\Delta k_x)^2 - (q\Delta k_y)^2. \tag{14c}$$

The detailed solution procedure to obtain Eq. (14) is presented in the Appendix. Similar to Eq. (13), homogeneous solutions are neglected in Eq. (14). Eq. (14) also satisfies the assumption that there is neither a reflective wave generated at the infinite boundary of the open 3-D space nor a nonlinear component at the source surface, i.e., $P_{22lq}(z_0)=0$. As in the dissipative sound pressure spectrum in Eq. (13b), the nonlinear sound spectrum, $P_{22lq}(z)$ includes the secular term that increases as z increases in the supersonic region.

The dissipative and nonlinear wave number spectra in Eqs. (13b) and (14b) are obtained from the second step in Fig. 2. Then, a renormalization procedure can be used to remove the secular terms and result in uniformly valid solutions (see Step 3a in Fig. 2 and Section 2.3). Another approach is applying spatial inverse Fourier transform to the spectra in Eqs. (13b) and (14b) to directly obtain the reconstructed sound pressure fields without the renormalization procedure (see Step 3b in Fig. 2). In Section 3.4, it is demonstrated that these two approaches result in almost identical reconstructed sound pressure fields in the nearfield of a pulsating sphere.

2.3. Renormalization

In order to obtain the uniformly valid solution of Eq. (4) at a large z value, the secular terms including the $(z-z_0) \cdot \exp(ik_z(z-z_0))$ term in Eqs. (13b) and (14b) are eliminated by using a renormalization procedure. From Eqs. (5), (13), and (14), the total sound pressure is written in a complex form as

$$p(x,y,z,t) = p_1(x,y,z)e^{-i\omega t} + p_{21}(x,y,z)e^{-i\omega t} + p_{22}(x,y,z)e^{-i2\omega t}. \tag{15}$$

In order to eliminate the secular terms in Eqs. (13b) and (14b), a strained coordinate, ζ is introduced as

$$z = \zeta + \varepsilon z_1(x,y,z,\zeta,t), \tag{16}$$

where ε is the small perturbation parameter (i.e., acoustic Mach number) and z_1 is the function determined to eliminate all the second-order small secular terms. When compared to the three strained coordinates defined in a 3-D space in Refs. [17,18], the only one strained coordinate is used in Eq. (16) to renormalize the secular terms. By substituting Eqs. (16) into (5), (13), and (14) and retaining up to the second-order terms, a condition for removing the secular terms is obtained: i.e., the strain coordinate, ζ can be found by setting the absolute value of the following renormalization function, f to zero for a given set of (x,y,z,t):

$$f(x,y,z,\zeta,t) = \frac{1}{N_x N_y} \sum_{l=0}^{N_x-1} \sum_{q=0}^{N_y-1} e^{il\Delta k_x x} e^{iq\Delta k_y y} \left[(z-\zeta) P_{1lq} ik_{zlq} e^{ik_{zlq}(\zeta-z_0)} e^{-i\omega t} \right.$$

$$\left. - \frac{ib\omega^3}{c_0^4} \frac{P_{1lq}}{2ik_{zlq}} (z-z_0) e^{ik_{zlq}(\zeta-z_0)} e^{-i\omega t} + \frac{2\beta\omega^2}{N_x N_y \rho_0 c_0^4} \frac{P_{1(l/2)(q/2)}^2}{2ik_{2zlq}} (z-z_0) e^{ik_{2zlq}(\zeta-z_0)} e^{-i2\omega t} \text{ when } l \text{ and } q \text{ are even} \right]. \tag{17}$$

The uniformly valid total sound pressure is then represented as

$$p(x,y,z,t) = \frac{1}{N_x N_y} \sum_{l=0}^{N_x-1} \sum_{q=0}^{N_y-1} e^{il\Delta k_x x} e^{iq\Delta k_y y} \left[P_{1lq} e^{ik_{zlq}(\zeta-z_0)} e^{-i\omega t} \right.$$

$$\left. + \frac{2\beta\omega^2}{N_x N_y \rho_0 c_0^4} \sum_{m=0}^{N_x-1} \sum_{n=0}^{N_y-1} P_{1mn} P_{1(l-m)(q-n)} \left(\frac{e^{i(k_{zmn}+k_{z(l-m)(q-n)})(\zeta-z_0)} - e^{ik_{2zlq}(\zeta-z_0)}}{(k_{2zlq})^2 - (k_{zmn}+k_{z(l-m)(q-n)})^2} \right) e^{-i2\omega t} \right], \tag{18}$$

where the subscripts, l and q satisfy $l \neq 2m$ or $q \neq 2n$. The nonlinear and dissipative sound pressure components are calculated by subtracting the linear NAH forward projected sound pressure from the total sound pressure in Eq. (18).

2.4. Nonlinear and dissipative pulsating sphere simulation

In this section, a pulsating sphere, with the radius of r_s, that radiates a nonlinear and dissipative sound pressure field is considered to validate the proposed nonlinear, dissipative, planar NAH procedure. Note that an acoustic monopole cannot be used to simulate the nonlinear and dissipative sound field since its infinitely small size compared to the smallest wave length makes it impossible to effectively radiate nonlinear sound fields [11]. Therefore, the radius, r_s, is here set to be in the same order of magnitude with the wave length, λ. The nonlinear and dissipative sound pressure field generated from the pulsating sphere is then obtained from the Burgers equation in the spherical coordinates, (r, θ, φ) with the assumption of the θ- and φ-direction symmetry conditions: i.e.,

$$\frac{\partial p}{\partial r} + \frac{p}{r} = \frac{b}{2c_0^3} \frac{\partial^2 p}{\partial \tau^2} + \frac{\beta p}{\rho_0 c_0^3} \frac{\partial p}{\partial \tau}, \tag{19}$$

where $\tau = t - (r-r_s)/c_0$ is the retarded time and r is the radial location $(r \geq r_s)$. Similar to the WWE, the spherical Burgers equation also describes cumulative nonlinear effects. According to the perturbation procedure presented in Section 2.1, the sound pressure, p in Eq. (19) is decomposed into multiple orders of magnitude (see Eq. (3)). By neglecting the third- and higher-order small terms, Eq. (19) can be decomposed into the following first- and second-order equations: i.e.,

$$\frac{\partial p_1}{\partial r} + \frac{p_1}{r} = 0, \tag{20}$$

$$\frac{\partial p_2}{\partial r} + \frac{p_2}{r} = \frac{b}{2c_0^3} \frac{\partial^2 p_1}{\partial \tau^2} + \frac{\beta p_1}{\rho_0 c_0^3} \frac{\partial p_1}{\partial \tau}. \tag{21}$$

Then, the total sound pressure solution is represented as

$$p(r,\tau) = \text{Re} \left(P_1 r_s \frac{e^{-i\omega\tau}}{r} + C_{1\omega} \frac{r-r_s}{r} e^{-i\omega\tau} + C_{2\omega} \frac{\ln(r/r_s)}{r} e^{-i2\omega\tau} \right), \tag{22a}$$

where P_1 is the acoustic pressure amplitude on the sphere surface at $r=r_s$ and $C_{1\omega}$ and $C_{2\omega}$ are the constants defined as

$$C_{1\omega} = -\frac{b}{2c_0^3} P_1 r_s \omega^2, \tag{22b}$$

$$C_{2\omega} = -i \frac{\omega\beta}{2\rho_0 c_0^3} P_1^2 r_s^2. \tag{22c}$$

When compared to the first-order sound pressure component, the second-order components in Eq. (22a) have the growing factors, $(r-r_s)$ and $\ln(r/r_s)$. Thus, the solution in Eq. (22) is not uniformly valid. These secular terms are thus removed by using the aforementioned renormalization procedure (see Section 2.3). Here, the strained coordinate, α is defined as

$$r = \alpha + \varepsilon r_1(r,\alpha,\tau),\tag{23}$$

where r_1 is determined to eliminate the second-order secular terms in Eq. (22). By plugging Eqs. (23) into (22), the renormalization function can be represented as

$$g(r,\alpha,\tau) = \frac{\mathrm{e}^{-\mathrm{i}\omega\tau}}{\alpha^2}\left[-P_1 r_s(r-\alpha) + \alpha C_{1\omega}(r-r_s) + \alpha C_{2\omega}\ln\left(\frac{r}{r_s}\right)\mathrm{e}^{-\mathrm{i}\omega\tau}\right].\tag{24}$$

Similar to Section 2.3, the complex strained coordinate, α can be obtained by setting the absolute value of Eq. (24) to zero for the given r and τ. The renormalized total sound pressure in Eq. (22a) is then represented in the form of complex sound pressure as

$$p(r,\tau) = P_1 r_s \frac{\mathrm{e}^{-\mathrm{i}\omega\tau}}{\alpha}.\tag{25}$$

This renormalized sound pressure includes both linear and nonlinear sound pressure components. The linear sound pressure data on the hologram surface ($z=z_h$) at the fundamental frequency of ω can be obtained from Eq. (25) by replacing α with $r=r_{hn}$ where r_{hn} represents the radial location of the nth receiver on the hologram surface. These hologram data are linearly backward projected to the source surface at $z=z_0$ and the reconstructed source sound pressure data are then used for the nonlinear, forward NAH projections. The linear and nonlinear sound pressure fields directly-calculated from Eq. (25) are compared with the reconstructed sound pressure fields to validate the projection performance of the proposed NAH procedure.

In addition to the pulsating sphere simulation, the 1-D nonlinear planar wave field radiated from an infinite-size panel is also calculated by solving the Burgers equation in the rectangular coordinates based on the aforementioned perturbation procedure. The directly-calculated nonlinear sound pressure field radiated from the infinite-size panel is then compared to the nonlinearly-reconstructed sound pressure field. Since the solution procedure to obtain the 1-D nonlinear planar wave is similar to the pulsating sphere case, it is not presented in this paper.

3. Numerical simulation results

3.1. Simulation setups

Fig. 3(a) shows the pulsating sphere simulation setup in a free field. The center of the pulsating sphere with the radius of $r_s=0.25$ m is placed at $(x,y,z)=(0.75,0.75,-0.25)$ m. The sound pressure amplitude of the pulsating sphere on its undisturbed surface at $r=0.25$ m is 6 kPa (i.e., 169.5 dB referenced at 20 μPa) and the excitation frequency is 1 kHz. A 31×31 acoustic pressure transducer array with the sampling intervals of $\Delta x=\Delta y=0.05$ m is placed at $z=0.05$ m to obtain hologram sound pressure data. Thus, the hologram height is 0.05 m when the plane on the pulsating sphere surface at $z=0$ m is defined as the source surface. The fundamental frequency component at 1 kHz contains the only first-order, linear sound pressures. Thus, in a "real" measurement, "linear" NAH measurement techniques, such as the scan-based, multi-reference NAH measurement technique and the partial field decomposition procedures [4–6], can be used for the proposed NAH procedure. Although a microphone with a large dynamic range (e.g., up to 170 dB) is usually expensive, a small number of such microphones can thus be used to conduct scanning measurements to cover a large measurement surface.

Fig. 3(b) presents the infinite-size panel simulation setup. The sound pressure magnitude on the panel surface is 1.2 kPa (i.e., 155.6 dB referenced at 20 μPa) and the excitation frequency is 1 kHz. The acoustic pressure transducer array has an increased size of 61×61 with the same sampling intervals of $\Delta x=\Delta y=0.05$ m as in the pulsating sphere simulation case. The panel is tilted by $4°$ around the y-axis and the hologram height is 0.05 m as shown in Fig. 3(b). The whole panel is assumed to be excited in phase with respect to its tilted position.

Since both the pulsating sphere and infinite-size panel can generate "cumulative" nonlinear sound waves with straight rays, the two simulations can be used to validate the proposed NAH procedure. In the following simulation and NAH projection results, an instant time, t is considered at the fundamental frequency of 1 kHz and the second harmonic of 2 kHz. Then, the absolute values of the resulting linear and nonlinear sound pressures obtained from Eqs. (18) and (25) are constant regardless of the time, t. The time-averaged sound pressure amplitudes (i.e., root-mean-square amplitudes) are thus obtained from the absolute values of the complex sound pressure amplitudes divided by the square root of 2.

3.2. Directly-calculated sound pressure fields

In order to calculate the sound pressure field radiated from the pulsating sphere by using Eq. (25), the strained coordinate, α, is first determined by numerically searching for the roots of $|g(r,\alpha,\tau)|=0$ in Eq. (24). For example, Fig. 4(a)
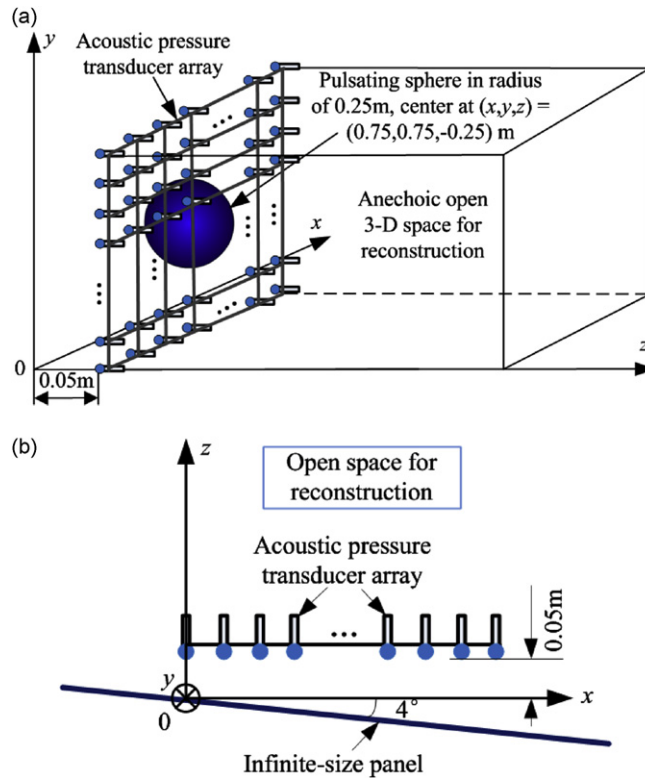
Fig. 3. Sketch of nonlinear, dissipative numerical simulation setups: (a) Pulsating sphere simulation, and (b) Infinite-size panel simulation.

shows the absolute value of the renormalization function, $g(r,\alpha,\tau)$ as the function of the real and imaginary parts of α at $r=1.25$ m. The root of $|g(r,\alpha,\tau)|=0$ can be identified from Fig. 4(a) and indicated in a circle in Fig. 4(a)–(c). Here, the root searching procedure is based on the assumptions that the strained coordinate, α is a continuous function and there is neither cumulative nor local nonlinear components on the stationary source surface at $r=0.25$ m: i.e., $\alpha_0=0.25$ at $r=0.25$ m, and α_n at $r_n=(n\Delta r+0.25)$ m is numerically searched with the initial solution of α_{n-1} ($n=1,2,3,...$). Fig. 4(b) and (c) shows the real and imaginary parts of $(\alpha-r)$, as a function of r, that exhibit periodic behaviors with the period of one wave length (i.e., $\lambda=0.34$ m at 1 kHz) while their amplitudes increase as r increases.

By using the strained coordinate, α in Fig. 4, the total (i.e., linear, nonlinear, and dissipative) sound pressure field is directly calculated from Eq. (25). The linear, lossless component that is obtained by replacing α with r in Eq. (25) is shown in Fig. 5(a) at the fundamental frequency of 1 kHz. The linear sound pressure amplitude in Fig. 5(a) decreases proportionally to $1/r$. The cumulative nonlinear sound pressure field is obtained by subtracting the linear and dissipative sound pressure from the total sound pressure (see Fig. 5(b)). The nonlinear sound pressure field in Fig. 5(b) has the minimum sound pressure level (SPL) at $(x,y,z)=(0.75,0.75,0)$ m (i.e., on the sphere surface at $r=0.25$ m) where the nonlinear SPL is approximately 115 dB. The nonlinear SPL is proportional to $\ln(r/r_s)/r$ and approximately 10 dB less than the linear SPL at $r=3$ m. The dissipative sound pressure field can be obtained by considering only the dissipative source term in Eq. (21) and following the identical perturbation and renormalization procedures as in Section 2.4 (see Fig. 5(c)). Fig. 5(c) shows that the dissipative sound pressure field has negligibly low SPL when compared with the linear and nonlinear sound pressure fields in Fig. 5(a) and (b).

3.3. Backward projected sound pressure fields

The sound pressure data calculated on the hologram surface at the fundamental frequency of 1 kHz is linearly backward projected onto the source surface. In order to reduce the truncation errors at the measurement aperture edges, the improved SONAH procedure [10] is used for this linear backward projection, which is indicated as Step 1 in Fig. 2.

Fig. 6(a) and (b) shows the directly-calculated sound pressure field and the linearly-backward-projected sound pressure field by using the improved SONAH procedure, respectively. The reconstructed sound pressure field matches well with the directly-calculated one (see the reconstruction error in Fig. 6(c)). Although the reconstruction error is relatively large approximately at 0.6 dB along the measurement aperture edges, a spatial window can be used to suppress this reconstruction error in the nonlinear forward NAH projections. The reconstructed sound pressure data on the source surface at $z=0$ m is input to the proposed nonlinear NAH projection procedure.
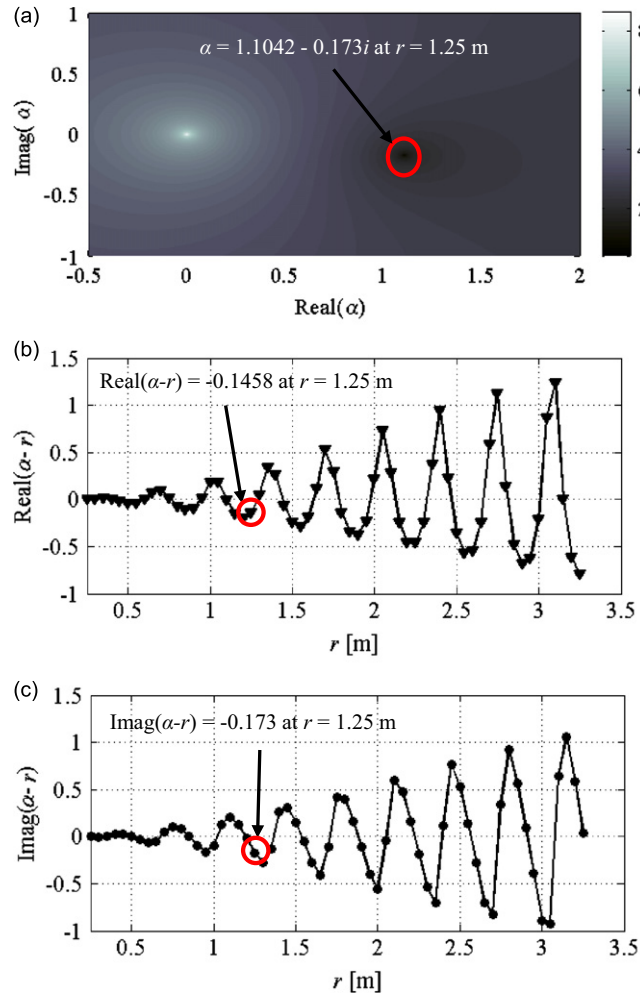
Fig. 4. Strained coordinate, α for pulsating sphere simulation: (a) Absolute values of renormalization function, $|g(r,\alpha,\tau)|$ at $r=1.25$ m, (b) real part of $(\alpha - r)$, and (c) imaginary part of $(\alpha - r)$.

3.4. Forward projected sound pressure fields

The sound pressures along the four reconstruction lines in Fig. 5(a) and (b) are reconstructed by using the proposed nonlinear NAH procedure. The reconstruction lines are selected in the nearfield of the pulsating sphere since the linear, forward NAH procedure is limited to nearfield reconstructions due to the farfield reconstruction error caused by spatial-FFT-induced ghost images [1–3]. The ghost image effects can be reduced by padding a large number of zeros around the source sound pressure data although computation time increases significantly due to the increased data size.

In order to reconstruct the sound pressures along the reconstruction lines from the linearly reconstructed source sound pressure, the strained coordinate, ζ in Eq. (16) is first determined by numerically searching for the roots of $|f(x,y,z,\zeta,t)|=0$ in Eq. (17) as in the pulsating sphere simulation case described in Section 3.2. Fig. 7(a)–(d) shows the real and imaginary parts of $(\zeta - z)$ along the four reconstruction lines. The results along reconstruction lines 1–3 in Fig. 7(a)–(c) show similar periodic behaviors as in the pulsating sphere case in Fig. 4(b) and (c) with the period of one wavelength.

Fig. 8(a)–(d) shows the directly-calculated and NAH-projected SPLs along reconstruction lines 1–4. Here, the NAH-projected "linear" SPLs are obtained by applying the conventional, linear NAH procedure to the source data as in Eq. (5) and the NAH-projected, cumulative "nonlinear" SPLs are calculated by subtracting the NAH-projected "linear" sound pressure components from the "total" components obtained from the renormalization procedure as in Eq. (18). Since the dissipative component is negligible (see Fig. 5), the subtraction of the linear component from the total sound pressure results in the nonlinear component dominantly. The NAH-projected, linear SPLs match well with the directly-calculated, linear SPLs along the all four reconstruction lines (see the dash lines with circular markers). The NAH-projected, nonlinear SPLs also match well with the directly-calculated, nonlinear SPLs along the reconstruction lines 3 and 4 (see the solid lines with triangle markers in Fig. 8(c) and (d)). Along off-centered reconstruction lines 1 and 2 in Fig. 8(a) and (b), the discrepancies between the directly-calculated and NAH-projected nonlinear components in the region close to the source
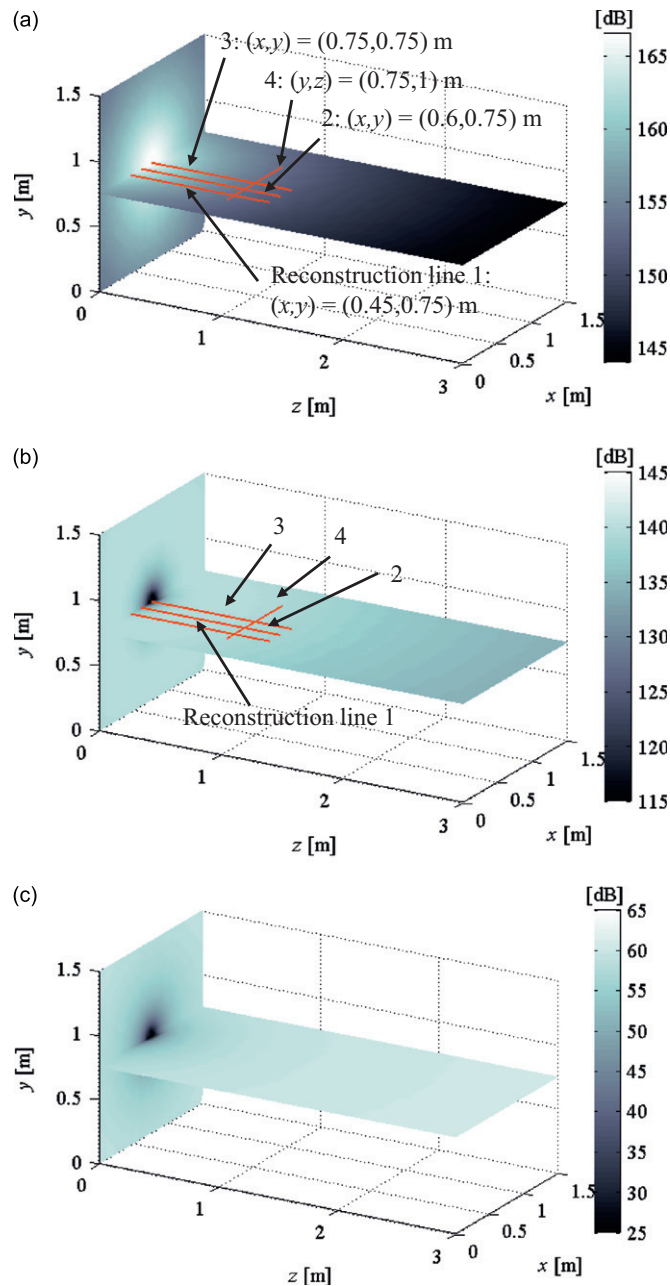
Fig. 5. 3-D sound pressure fields directly-calculated from pulsating sphere on x–y plane at $z=0$ m and x–z plane at $y=0.75$ m when excited at 1 kHz: (a) linear, lossless sound pressure field, (b) corresponding nonlinear sound pressure field at 2 kHz, and (c) corresponding dissipative sound pressure field at 1 kHz.

surface at $z=0$ m are caused by the assumption of no nonlinear component at the source surface, although the pulsating sphere simulation results in the cumulative nonlinear components at the source surface (see Fig. 5(b)). However, these discrepancies decrease as z increases.

Fig. 9(a)–(d) shows the reconstruction errors that are defined as the SPL differences between the directly-calculated and NAH-projected SPLs in Fig. 8. Along off-centered reconstruction lines 1 and 2, Fig. 9(a) and (b) shows that the nonlinear NAH reconstruction errors represented by the solid lines with the triangle markers decrease quickly around the source surface as z increases. Along reconstruction line 3 at the center of the measurement aperture, the nonlinear reconstruction error is within 0.2 dB, while the linear reconstruction error represented by the dash line with circular markers increases oscillatory as z increases with the maximum error of approximately 0.35 dB at $z=1.2$ m. The latter indicates that the spatial-FFT-induced ghost image effects and the measurement aperture truncation errors become more significant as z
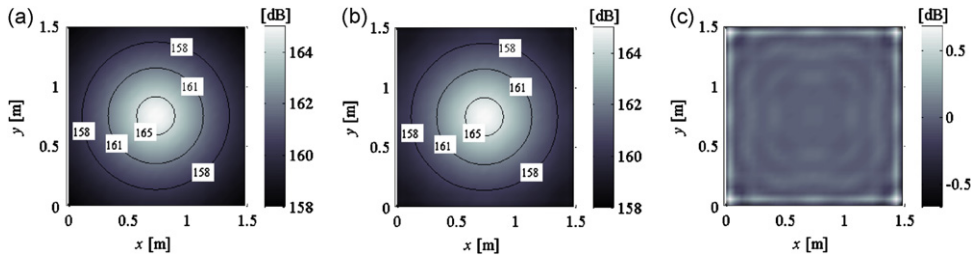
Y. Niu, Y.-J. Kim / Journal of Sound and Vibration 332 (2013) 952–967

Fig. 6. Linear sound pressure fields on x–y plane at $z=0$ m: (a) directly-calculated sound pressure field, (b) SONAH-reconstructed sound pressure field, and (c) reconstruction error (i.e., dB differences between reconstructed and directly-calculated sound pressure levels (SPLs)).
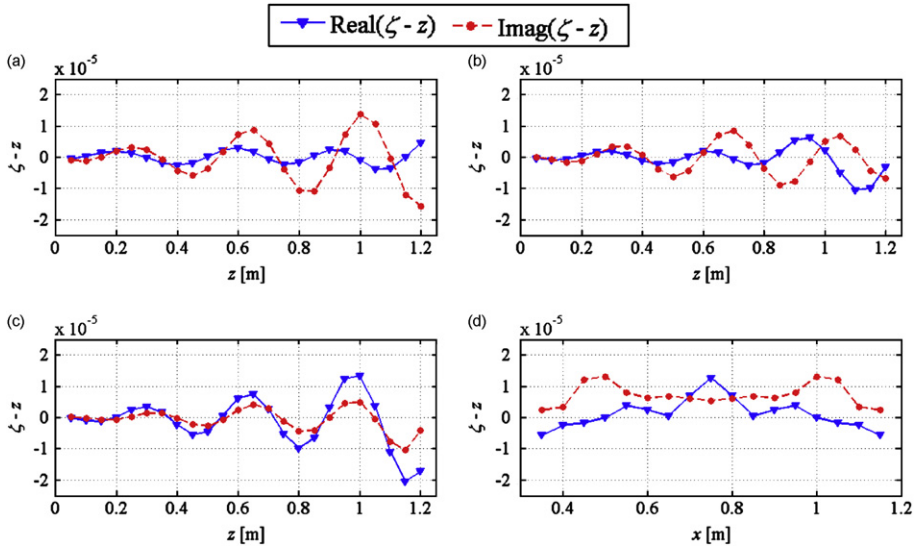

Fig. 7. Real and imaginary parts of strained coordinate fluctuation, $(\zeta-z)$ along reconstruction lines 1–4: (a) reconstruction line 1, (b) reconstruction line 2, (c) reconstruction line 3, and (d) reconstruction line 4.
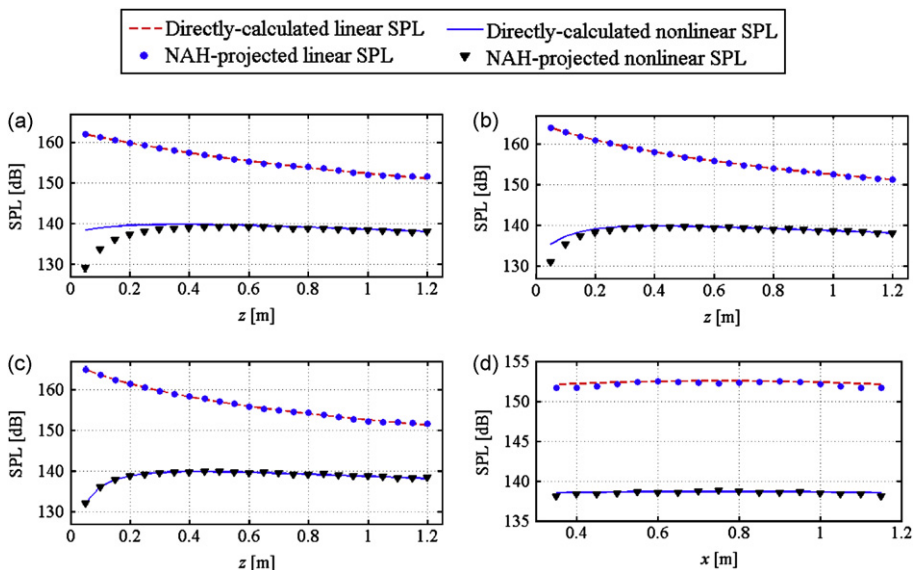

Fig. 8. Directly-calculated and NAH-projected SPLs along reconstruction lines 1–4: (a) reconstruction line 1, (b) reconstruction line 2, (c) reconstruction line 3, and (d) reconstruction line 4.
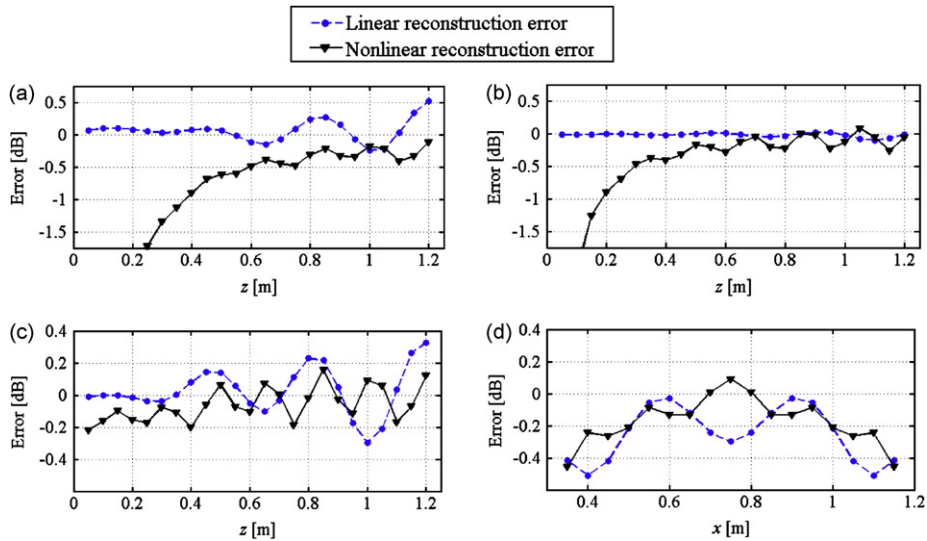
Fig. 9. NAH reconstruction errors along reconstruction lines 1–4: (a) reconstruction line 1, (b) reconstruction line 2, (c) reconstruction line 3, and (d) reconstruction line 4.
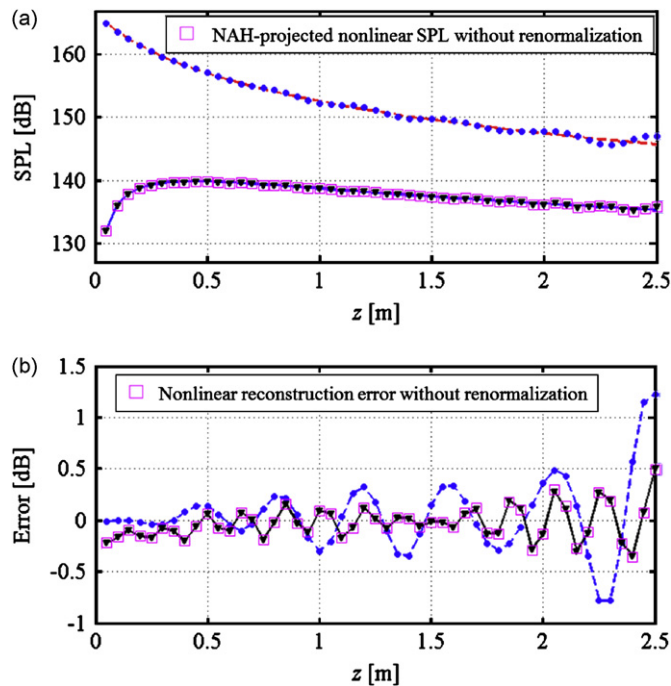

Fig. 10. Reconstruction results with and without renormalization along reconstruction line 3 extended up to $z=2.5$ m (The line and marker legends are same as Figs. 8 and 9 except no renormalization case): (a) directly-calculated and NAH-projected linear and nonlinear SPLs, and (b) reconstruction errors.

increases further from the pulsating sphere [1–3]. Along reconstruction line 4, Fig. 9(d) shows that both the linear and nonlinear NAH reconstruction errors are approximately 0.1–0.3 dB around the center at $x=0.75$ m and become larger (e.g., up to approximately 0.5 dB) as the reconstruction location is further away from the center to the measurement aperture edges where the aperture edge truncation errors and the ghost image effects are more significant than those at the center.

The small magnitudes of the strained coordinate fluctuation, $(\zeta - z)$ in Fig. 7 indicate that the secular terms in Eqs. (13b) and (14b) are negligible in Eqs. (15) and (18) for the given reconstruction space. Thus, Eqs. (13) and (14) can be directly applied for the nonlinear and dissipative NAH projections without renormalizing these equations (see Step 3b in Fig. 2) although the renormalization procedure is necessary for long distance farfield projections.

Fig. 10(a) and (b) shows the effects of the renormalization along reconstruction line 3 extended up to $z=2.5$ m (i.e., $z \cong 7.3\lambda$ where λ is the wave length at 1 kHz). The same line and marker legends in Figs. 8 and 9 are reused in Fig. 10

except no renormalization case. The NAH-projected, nonlinear SPL and reconstruction error without the renormalization are represented by hollow square markers. In Fig. 10(a), as z increases farther from the source surface at $z=0$ m, the nonlinear component becomes relatively significant compared to the linear component: i.e., the SPL difference between the linear and nonlinear components becomes small as z increases. In Fig. 10(b), the linear reconstruction error represented by the dash line with circular markers increases oscillatory up to 1.2 dB at $z=2.5$ m. The latter indicates that the spatial-FFT-induced ghost image effects and the measurement aperture truncation errors become much more significant as the reconstruction distance, z increases much further from the source, although the edges of the source data are smoothed by applying the spatial Tukey window with the 50 percent flat top and the source data are zero-padded with $8N_x \times 8N_y$ zeros. The nonlinear reconstruction error of the no renormalization case (i.e., the hollow rectangular markers) in Fig. 10(b) has almost identical values with that of the renormalization case represented by the solid line with triangle markers. The maximum nonlinear reconstruction error is approximately 0.5 dB at $z=2.5$ m.

For no renormalization procedure case, the directly-calculated and reconstructed "linear" sound pressure fields and the reconstruction errors are shown in Fig. 11 on the x–y plane at $z=1.25$ m and the x–z plane at $y=0.75$ m. The sound pressure fields in linear scales in Fig. 11 are obtained from the real parts of Eqs. (25) and (18) by considering the only linear
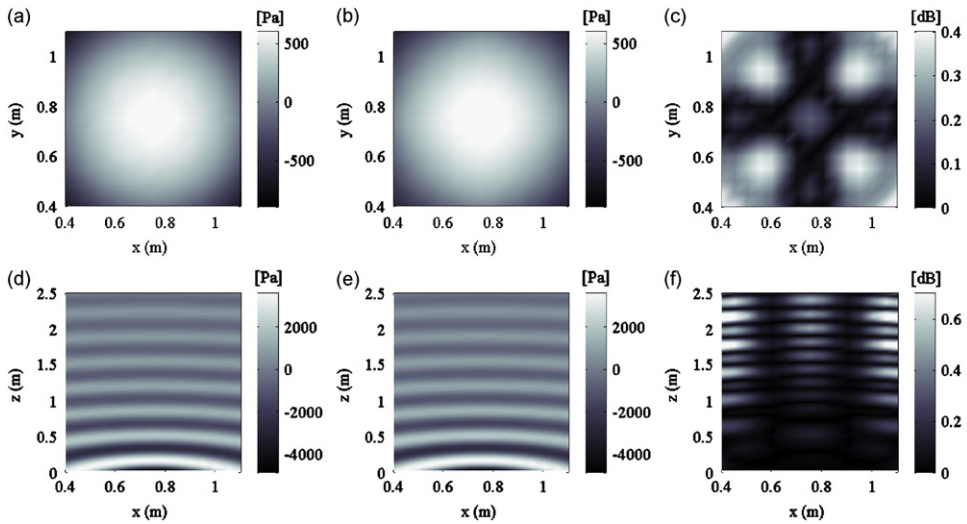

Fig. 11. Directly-calculated and NAH-projected "linear" sound pressure fields from pulsating "sphere" on x–y plane at $z=1.25$ m and x–z plane at $y=0.75$ m: (a) directly-calculated on x–y plane, (b) reconstructed on x–y plane, (c) reconstruction error on x–y plane, (d) directly-calculated on x–z plane, (e) reconstructed on x–z plane, and (f) reconstruction error on x–z plane.

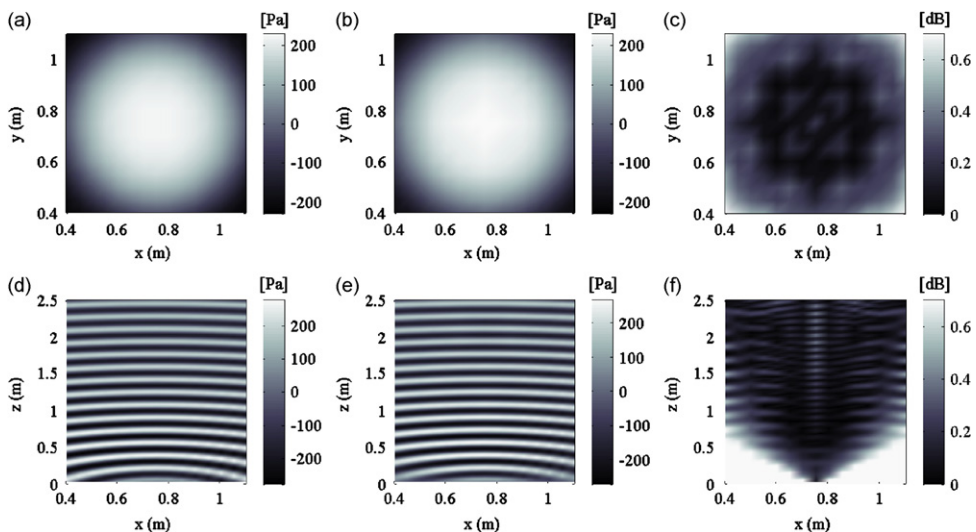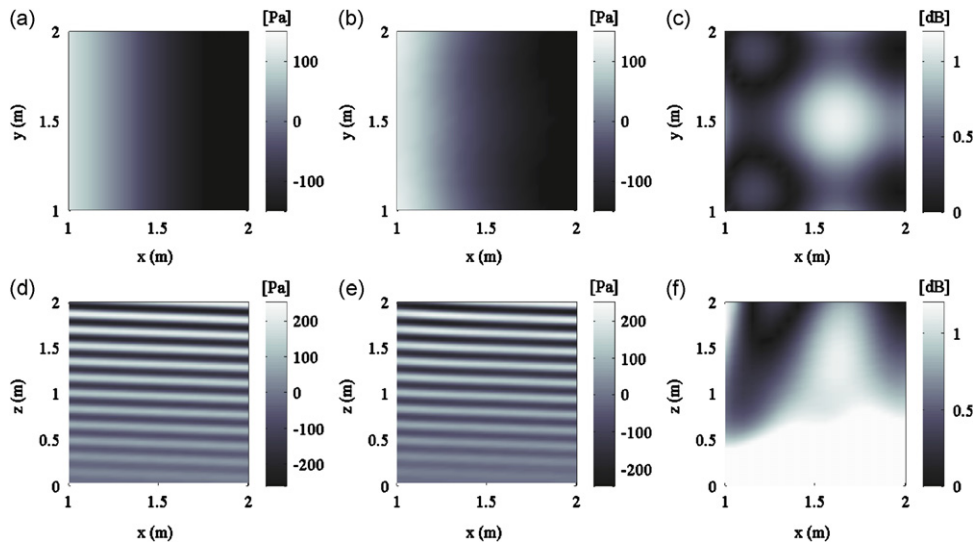
Fig. 12. Directly-calculated and NAH-projected "nonlinear" sound pressure fields from pulsating "sphere" on x–y plane at $z=1.25$ m and x–z plane at $y=0.75$ m: (a) directly-calculated on x–y plane, (b) reconstructed on x–y plane, (c) reconstruction error on x–y plane, (d) directly-calculated on x–z plane, (e) reconstructed on x–z plane, and (f) reconstruction error on x–z plane.

Fig. 13. Directly-calculated and NAH-projected "nonlinear" sound pressure fields from infinite-size "panel" on x–y plane at $z=1.25$ m and x–z plane at $y=1.5$ m: (a) directly-calculated on x–y plane, (b) reconstructed on x–y plane, (c) reconstruction error on x–y plane, (d) directly-calculated on x–z plane, (e) reconstructed on x–z plane, and (f) reconstruction error on x–z plane.

and lossless components. The reconstructed sound pressure fields at 1 kHz agree well with the directly-calculated ones (see the reconstruction errors in Fig. 11(c) and (f)). Similar to the linear reconstruction error shown in Fig. 10(b), the linear NAH reconstruction errors on the x–z plane in Fig. 11(f) increase as z increases due to the ghost image effects and measurement aperture edge truncation errors.

Fig. 12 shows the directly-calculated and reconstructed "nonlinear" sound pressure fields at 2 kHz and the reconstruction errors on the same surfaces as in Fig. 11. The well matched nonlinear sound pressure fields in Fig. 12(a), (b), (d), and (e) as well as the small reconstruction errors with the maximum SPL difference of 0.6 dB in Fig. 12(c) and (f) successfully validate the projection performance of the proposed nonlinear NAH procedure in the spherical wave simulation. In Fig. 12(f), the discrepancies at the off-centered locations close to the source surface at $z=0$ m are caused by the assumption of no nonlinearity on the source plane, as described in Fig. 8(a) and (b).

Similar to Fig. 12, Fig. 13 shows the directly-calculated and NAH-predicted "nonlinear" sound pressure fields and the reconstruction errors for the infinite-size "panel" simulation. Here, the x–y plane is chosen at $z=1.25$ m, and the x–z plane is placed at $y=1.5$ m. The directly-calculated and NAH-projected nonlinear sound pressure fields agree well with each other on both the planes (see the reconstruction errors in Fig. 13(c) and (f)). Except the regions close to the planar source plane at $z=0$ m where zero-nonlinearity assumption is imposed, the maximum reconstruction error in Fig. 13(c) and (f) is approximately 1 dB. Thus, the reconstruction performance of the proposed nonlinear NAH procedure is also validated through the infinite-size panel simulation.

4. Conclusions

In this paper, the novel, nonlinear, dissipative, planar NAH algorithm is introduced that is based on the first- and second-order perturbation solutions of the Westervelt wave equation (WWE) and the modified renormalization procedure. The proposed NAH procedure is applicable to cumulative nonlinearity dominant sound fields with straight rays such as spherical waves and 1-D planar waves. By using the perturbation method, the WWE is decomposed into the first- and second-order wave equations. The conventional, linear, planar NAH technique is applied to solve the first-order wave equation. The resulting linear sound pressure solution is input to the second-order wave equation as the inhomogeneous source terms to find the second-order, nonlinear sound pressure solutions. The secular terms in the second-order solutions are removed by using the modified renormalization approach to obtain the uniformly valid solution.

By applying the aforementioned perturbation and renormalization procedures to the spherical Burgers equation, the sound pressure field radiated from the high-level pulsating sphere is calculated to validate the proposed NAH algorithm. In the nearfield of the pulsating sphere up to $z=1.2$ m$=3.5\lambda$, the SPLs reconstructed by using the proposed NAH procedure match well with the directly-calculated SPLs along the four reconstruction lines. The maximum reconstruction errors are approximately 0.3 dB for the linear NAH projections and 0.2 dB for the nonlinear NAH projections.

Along the centered reconstruction line, as z value increases farther from the sound source surface up to $z=2.5$ m$=7.3\lambda$, the spatial-FFT-based linear reconstruction solution suffers from the more significant spatial-FFT-induced ghost image effects and the measurement aperture truncation errors, which increase the linear reconstruction error up to 1.2 dB. Then,

this linear reconstruction error degrades the performance of the proposed nonlinear NAH procedure with the maximum reconstruction error of 0.5 dB.

In addition to the NAH results along the reconstruction lines, the sound pressure fields generated from the pulsating sphere and infinite-size vibrating panel are reconstructed in the 3-D space and compared to the directly-calculated sound pressure fields. The nonlinear NAH reconstruction results agree well with the exact ones at the maximum reconstruction errors of 0.6 dB and 1 dB, respectively, for the pulsating sphere and infinite-size panel simulations. Thus, through both the pulsating sphere and infinite-size panel simulations, it can be concluded that the reconstruction performance of the proposed NAH procedure is successfully validated.

In the proposed nonlinear NAH projections, the secular terms have negligible effects on the uniformly valid solutions. Thus, it can be also concluded that the proposed nonlinear and dissipative NAH procedure can be applied to reconstruct the sound pressure fields successfully in the nearfields of the sound sources regardless of the renormalization procedure.

Acknowledgment

Appendix A

The detailed procedure for deriving the solution of Eq. (12) is presented in this appendix. By plugging Eqs. (14a) to (12) and considering arbitrary l and q terms, the inhomogeneous second-order ordinary differential equation can be obtained as

$$\frac{d^2 P_{22lq}}{dz^2} + k_{2zlq}^2 P_{22lq} = \frac{2\beta\omega^2}{N_x^2 N_y^2 \rho_0 c_0^4} \left[\sum_{m=0}^{N_x-1} \sum_{n=0}^{N_y-1} P_{1mn} P_{1(l-m)(q-n)} e^{i\left(k_{zmn} + k_{z(l-m)(q-n)}\right)(z-z_0)} \right] = B_{lq}(z). \tag{A1}$$

The particular solution to Eq. (A1) is obtained by using the variation of parameters as

$$P_{22lq} = -e^{ik_{2zlq}(z-z_0)} \int_{z_0}^{z} \frac{e^{-ik_{2zlq}(z-z_0)} B_{lq}(z)}{W_{lq}} dz + e^{-ik_{2zlq}(z-z_0)} \int_{z_0}^{z} \frac{e^{ik_{2zlq}(z-z_0)} B_{lq}(z)}{W_{lq}} dz, \tag{A2}$$

where the Wronskian W_{lq} is

$$W_{lq} = e^{ik_{2zlq}(z-z_0)} \frac{de^{-ik_{2zlq}(z-z_0)}}{dz} - \frac{de^{ik_{2zlq}(z-z_0)}}{dz} e^{-ik_{2zlq}(z-z_0)} = -2ik_{2zlq}. \tag{A3}$$

Therefore, Eq. (A2) can be written as the combination of homogeneous and particular solutions for the case of $l \neq 2m$ or $q \neq 2n$: i.e.,

$$P_{22lq}(z) = \frac{2\beta\omega^2}{2ik_{2zlq} N_x^2 N_y^2 \rho_0 c_0^4} \sum_{m=0}^{N_x-1} \sum_{n=0}^{N_y-1} P_{1mn} P_{1(l-m)(q-n)} \left[\frac{2ik_{2zlq} e^{i\left(k_{zmn}+k_{z(l-m)(q-n)}\right)(z-z_0)}}{(k_{2zlq})^2 - (k_{zmn}+k_{z(l-m)(q-n)})^2} \right.$$
$$\left. + \frac{i\left(k_{zmn}+k_{z(l-m)(q-n)}\right)\left(e^{-ik_{2zlq}(z-z_0)} - e^{ik_{2zlq}(z-z_0)}\right)}{(k_{2zlq})^2 - (k_{zmn}+k_{z(l-m)(q-n)})^2} - \frac{2ik_{2zlq}\left(e^{-ik_{2zlq}(z-z_0)} + e^{ik_{2zlq}(z-z_0)}\right)}{(k_{2zlq})^2 - (k_{zmn}+k_{z(l-m)(q-n)})^2} \right]. \tag{A4}$$

The last two terms in the square bracket can be ignored since they are homogeneous solutions. However, the function $\exp(ik_{2zlq}(z-z_0))$ with the coefficient of $2ik_{2zlq}$ in the third term is retained to satisfy the $P_{22lq}(z_0)=0$ condition (i.e., no nonlinearity condition on the source surface), while the $\exp(-ik_{2zlq}(z-z_0))$ term is discarded due to its exponentially increasing nature when k_{2zlq} is imaginary: i.e.,

$$P_{22lq}(z) = \frac{2\beta\omega^2}{N_x^2 N_y^2 \rho_0 c_0^4} \sum_{m=0}^{N_x-1} \sum_{n=0}^{N_y-1} P_{1mn} P_{1(l-m)(q-n)} \left[\frac{e^{i\left(k_{zmn}+k_{z(l-m)(q-n)}\right)(z-z_0)} - e^{ik_{2zlq}(z-z_0)}}{(k_{2zlq})^2 - (k_{zmn}+k_{z(l-m)(q-n)})^2} \right] \quad \text{when } l \neq 2m \text{ or } q \neq 2n. \tag{A5}$$

For the case of $l=2m$ and $q=2n$, the wave numbers can be related as

$$(k_{2zlq})^2 = (k_{zmn}+k_{z(l-m)(q-n)})^2 = 4(k_{zmn})^2, \text{ when } l=2m \text{ and } q=2n.$$

Then, the solution of Eq. (A2) becomes

$$P_{22lq}(z) = \frac{2\beta\omega^2}{N_x^2 N_y^2 \rho_0 c_0^4} \frac{(z-z_0)e^{ik_{2zlq}(z-z_0)}}{2ik_{2zlq}} P_{1(l/2)(q/2)}^2 \quad \text{when } l=2m \text{ and } q=2n. \tag{A6}$$

Thus, the nonlinear wave number spectrum P_{22lq} in Eq. (14b) is obtained as in Eqs. (A5) and (A6).

References

[1] J.D. Maynard, E.G. Williams, Y. Lee, Nearfield acoustic holography: I. Theory of generalized holography and the development of NAH, Journal of the Acoustical Society of America 78 (1985) 1395–1413.

[2] W.A. Veronesi, J.D. Maynard, Nearfield acoustic holography (NAH): II. Holographic reconstruction algorithms and computer implementation, *Journal of the Acoustical Society of America* 81 (1987) 1307–1322.
[3] E.G. Williams, *Fourier Acoustics: Sound Radiation and Nearfield Acoustical Holography*, Academic, San Diego, CA, 1999.
[4] J. Hald, STSF—A Unique Technique for Scan-Based Nearfield Acoustical Holography Without Restriction on Coherence. Brüel & Kjær Technical Review No. 1 (1989), pp. 1–50.
[5] Y.-J. Kim, J.S. Bolton, H.-S. Kwon, Partial sound field decomposition in multireference near-field acoustical holography by using optimally located virtual references, *Journal of the Acoustical Society of America* 115 (2004) 1641–1652.
[6] H.-S. Kwon, Y.-J. Kim, J.S. Bolton, Compensation for source nonstationarity in multireference, scan-based near-field acoustical holography, *Journal of the Acoustical Society of America* 113 (2003) 360–368.
[7] J. Hald, Patch Near-Field Acoustical Holography Using a New Statistically Optimal Method. Brüel & Kjær Technical Review No. 1 (2005) pp. 40–50.
[8] E.G. Williams, B.H. Houston, P.C. Herdic, Fast Fourier Transform and singular value decomposition formulation for patch nearfield acoustic holography, *Journal of the Acoustical Society of America* 114 (2003) 1322–1333.
[9] H.-S. Kwon, Y. Niu, Y.-J. Kim, Planar nearfield acoustical holography in moving fluid medium at subsonic and uniform velocity, *Journal of the Acoustical Society of America* 128 (2010) 1823–1832.
[10] Y.-J. Kim, Y. Niu, Improved statistically optimal nearfield acoustical holography in subsonically moving fluid medium, *Journal of Sound and Vibration* 331 (2012) 3945–3960.
[11] M.F. Hamilton, D.T. Blackstock, *Nonlinear Acoustics*, Academic, San Diego, CA, 1998.
[12] M.J. Lighthill, Viscosity effects in sound waves of finite amplitude, in: G.K. Batchelor, R.M. Davies (Eds.), *Surveys in Mechanics*, Cambridge University Press, Cambridge, England1956, pp. 249–350.
[13] P.J. Westervelt, Parametric acoustic array, *Journal of the Acoustical Society of America* 35 (1963) 535–537.
[14] F.H. Fenlon, Derivation of the multiple frequency Bessel–Fubini series via Fourier analysis of the preshock time waveform, *Journal of the Acoustical Society of America* 53 (1973) 1752–1754.
[15] J.H. Ginsberg, Multi-dimensional non-linear acoustic wave propagation. Part II: the non-linear interaction of an acoustic fluid and plate under harmonic excitation, *Journal of Sound and Vibration* 40 (1975) 359–379.
[16] J.H. Ginsberg, A re-examination of the non-linear interaction between an acoustic fluid and a flat plate undergoing harmonic excitation, *Journal of Sound and Vibration* 60 (1978) 449–458.
[17] J.H. Ginsberg, Propagation of nonlinear acoustic waves induced by a vibrating cylinder. I. The two-dimensional case, *Journal of the Acoustical Society of America* 64 (1978) 1671–1678.
[18] J.H. Ginsberg, Propagation of nonlinear acoustic waves induced by a vibrating cylinder. II. The three-dimensional case, *Journal of the Acoustical Society of America* 64 (1978) 1679–1687.
[19] S.G. Kelly, A.H. Nayfeh, Non-linear interactions of acoustic fields with plates under harmonic excitations, *Journal of Sound and Vibration* 60 (1978) 371–377.
[20] A.H. Nayfeh, Non-linear propagation of waves induced by general vibrations of plates, *Journal of Sound and Vibration* 79 (1981) 429–437.
[21] S.G. Kelly, A.H. Nayfeh, Non-linear propagation of directional spherical waves, *Journal of Sound and Vibration* 72 (1980) 25–37.